Intermetallics 50 (2014) 94–107

Contents lists available at ScienceDirect

Intermetallics

journal homepage: www.elsevier.com/locate/intermet

Mechanical and functional behavior of a Ni-rich $Ni_{50.3}Ti_{29.7}Hf_{20}$ high temperature shape memory alloy

O. Benafan [a,*], A. Garg [b,a], R.D. Noebe [a], G.S. Bigelow [a], S.A. Padula II [a], D.J. Gaydosh [c,a], N. Schell [d], J.H. Mabe [e], R. Vaidyanathan [f]

[a] NASA Glenn Research Center, Structures and Materials Division, Cleveland, OH 44135, USA
[b] University of Toledo, Toledo, OH 43606, USA
[c] Ohio Aerospace Institute, Cleveland, OH 44142, USA
[d] Institute of Materials Research, Helmholtz-Zentrum Geesthacht, Max-Planck-Str. 1, D-21502 Geesthacht, Germany
[e] The Boeing Company, Seattle, WA 98124, USA
[f] Advanced Materials Processing and Analysis Center, Materials Science and Engineering Department, University of Central Florida, Orlando, FL 32816, USA

ARTICLE INFO

Article history:
Received 17 December 2013
Received in revised form
4 February 2014
Accepted 7 February 2014
Available online

Keywords:
B. Shape-memory effects
F. Diffraction
B. Precipitates
B. Phase transformation
A. Intermetallics
F. Mechanical testing

ABSTRACT

The mechanical and functional behaviors of a Ni-rich $Ni_{50.3}Ti_{29.7}Hf_{20}$ high temperature shape memory alloy were investigated through combined *ex situ* macroscopic experiments and *in situ* synchrotron X-ray diffraction. Isothermal tension and compression tests were conducted between room temperature and 260 °C, while isobaric thermomechanical cycling experiments were conducted at selected stresses up to 700 MPa. Isothermal testing of the martensite phase revealed no plastic strain up to the test limit of 1 GPa and near-perfect superelastic behavior up to 3% applied strain at temperatures above the austenite finish. Excellent dimensional stability with greater than 2.5% actuation strain without accumulation of noticeable residual strains (at stresses less than or equal to −400 MPa) were observed during isobaric thermal cycling experiments. The absence of residual strain accumulation during thermomechanical cycling was confirmed by the lattice strains, determined from X-ray spectra. Even in the untrained condition, the material exhibited little or no history or path dependence in behavior, consistent with measurements of the bulk texture after thermomechanical cycling using synchrotron X-ray diffraction. Post deformation cycling revealed the limited conditions under which a slight two-way shape memory effect (TWSME) was obtained, with a maximum of 0.34% two-way shape memory strain after thermomechanical cycling under −700 MPa.

Published by Elsevier Ltd.

1. Introduction

High temperature shape memory alloys (HTSMAs) have vast potential in a wide range of applications spanning the aerospace, automotive, and energy exploration industries, amongst others. The majority of these applications demand large actuation capability, higher transformation temperatures (above 100 °C) and stable responses, which restricts existing possibilities to a small group of alloys. Of these alloys, NiTi-based HTSMAs such as NiTiPd [1,2], NiTiPt [3,4], NiTiZr [5,6] and NiTiHf [6–12] have shown significant scientific and technological merit in the last few years. A comprehensive review of select HTSMAs can be found in Ref. [13]. In particular, NiTiHf has been developed as a low cost alternative when compared to NiTi-*X* (*X* = Pt, Pd, Au), and just recently, Ni-rich NiTiHf alloys were found to exhibit superior properties and dimensional stability through compositional and aging control [7–12,14,15]. This was accomplished by developing a slightly Ni-rich composition with 20 at.% Hf, that is capable of being precipitation strengthened when subjected to an aging heat treatment to produce fine, nanometer size precipitates. The precipitates strengthen the alloy providing high resistance to dislocation motion while allowing a nearly unobstructed phase transformation. Thus, it is useful to characterize both the macroscopic and microstructural behavior of Ni-rich NiTiHf to optimize the alloy and its processing, and to develop an appropriate database of properties to transition this material into engineering components.

The Ni-rich $Ni_{50.3}Ti_{29.7}Hf_{20}$ (at.%) alloy studied in this work exhibits a monoclinic B19′ martensite phase at room temperature and a cubic B2 austenite phase at 300 °C, as described in detail in Ref. [7]. Previously, the shape memory and superelastic behaviors of this alloy were determined under tension and compression for a

* Corresponding author. Tel.: +1 (216) 433 8538; fax: +1 (216) 977 7132.
E-mail address: othmane.benafan@nasa.gov (O. Benafan).

http://dx.doi.org/10.1016/j.intermet.2014.02.006
0966-9795/Published by Elsevier Ltd.

limited number of thermomechanical/mechanical cycles [10]. Similarly, compressive testing was performed on the same alloy at temperatures above the austenite finish (A_f) temperature to study the effect of aging on the stress-induced transformation and plasticity, but also only for a few cycles [8]. In single crystal form, the effects of applied stress and testing temperatures were evaluated along the [111] orientation with stress levels up to 1000 MPa [9]. From a microscopic perspective, *in situ* neutron diffraction was used to investigate the role of the fine precipitates on texture, internal strains, and other microstructural features during tensile and isobaric thermomechanical testing [7]. In all cases [7–10], the alloy exhibited outstanding strength and stability (lack of residual strain) during transformation under isothermal and isobaric conditions. The crystal structure of the precipitate phase, responsible for these benefits, has recently been described in detail by Yang et al. [14] and Santamarta et al. [6] using advanced characterization techniques and *ab-initio* calculations.

The promising results presented in the aforementioned references are the motivation behind the current effort to further examine the mechanical and functional limits of this alloy. The goal is two-fold: first to perform thermomechanical tests to an extended number of cycles in isothermal and isobaric modes to quantify the durability of this material for use in longer-life applications and second to conduct compressive thermomechanical testing using *in situ* synchrotron X-ray diffraction to assess any changes in the alloy's internal state and microstructure. Special attention is directed towards quantifying the microstructural reversibility of the transformation through changes in texture and lattice strains as a function of stress.

2. Material and methods

2.1. Material

The material used in this investigation was part of a larger heat of Ni-rich $Ni_{50.3}Ti_{29.7}Hf_{20}$ (at.%) alloy produced by Flowserve Corporation, Dayton, Ohio. The cast ingots were vacuum homogenized at 1050 °C for 72 h, followed by extrusion at 900 °C. Mechanical test specimens were machined from the extruded rods (HF202 and HF206) and subjected to an aging treatment of 3 h at 550 °C followed by furnace cooling to promote the formation of a high density of fine precipitate phase in the microstructure. This composition and heat treatment were selected based on previous studies [10,11], and after an extensive in-house optimization study of different compositions and aging temperatures/times that provided the best thermomechanical properties. Various physical and thermomechanical properties of heat-treated alloys of similar composition are available in the literature [7–10,14].

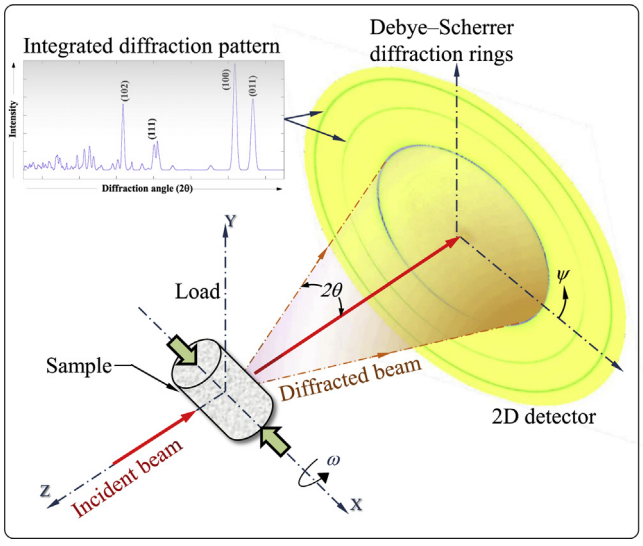

Fig. 1. Schematic illustration of the experimental diffraction setup.

2.2. Microstructural characterization

Microstructure of the extruded and aged material was analyzed using optical microscopy, scanning electron microscopy (SEM), and transmission electron microscopy (TEM) techniques. Samples for optical and SEM were mounted, polished and etched lightly using a solution of 85% H_2O, 12% HNO_3 and 3% HF (by volume) to reveal grain size. Transmission electron microcopy was accomplished using a double tilt holder in a FEI CM200 microscope operating at 200 kV. Samples for TEM were prepared from a 3 mm diameter cylinder that was electro-discharge machined from the extruded

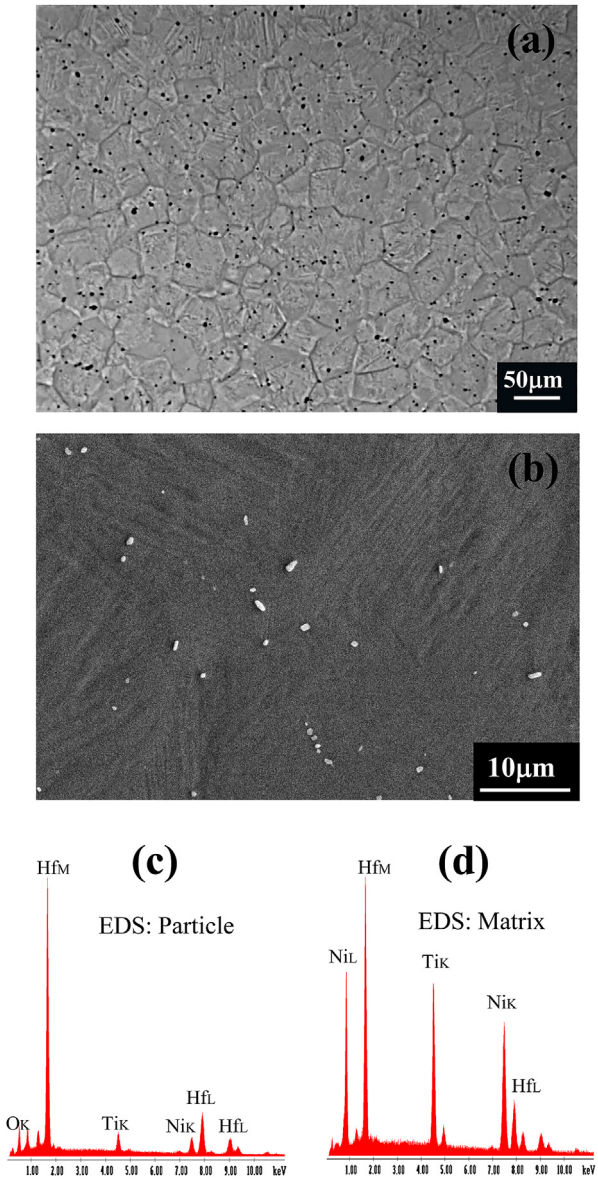

Fig. 2. Optical micrograph showing grain size and martensite twins, (b) SEM micrograph showing HfO_2 particles in a martensite matrix, (c) energy-dispersive X-ray spectroscopy (EDS) of lighter particles showing enrichment of Hf and O, (d) EDS of nearby matrix for comparison to (c).

and aged material. Disks of ~500 μm thickness were sectioned from this cylinder, mechanically ground to ~130 μm thickness, and then electro-polished using a solution of 20% sulfuric acid and 80% methanol (by volume) cooled to 0 °C in a Struers Tenupol-5 twin-jet electropolisher. TEM images, diffraction patterns, and energy dispersive spectra were collected and analyzed at room temperature to assess the initial microstructure of the extruded and aged material.

2.3. Isothermal mechanical and isobaric thermomechanical characterization

All *ex situ* mechanical testing was conducted using an MTS servohydraulic load frame. Prior to any testing, cylindrical threaded specimens (5.08 mm in diameter and 15.24 mm in gage length) were subjected to two stress-free thermal cycles between 30 and 300 °C, performed on the test frame, to relieve any residual stresses resulting from the machining operations. Macroscopic strains were measured using a 12.7 mm gage, high-temperature extensometer, while heating was controlled using an Ameritherm induction heating system. In all the experiments, a heating rate of 20 °C/min was used, and cooling was achieved through the water-cooled grips. The transformation temperatures: martensite start (M_s), martensite finish (M_f), austenite start (A_s), and austenite finish (A_f) were determined from the stress-free, strain–temperature response and were 142, 126, 155, and 169 ± 2 °C, respectively. Isothermal tests consisted of applying tensile or compressive stresses up to 1 GPa at temperatures from 30 to 300 °C, in strain

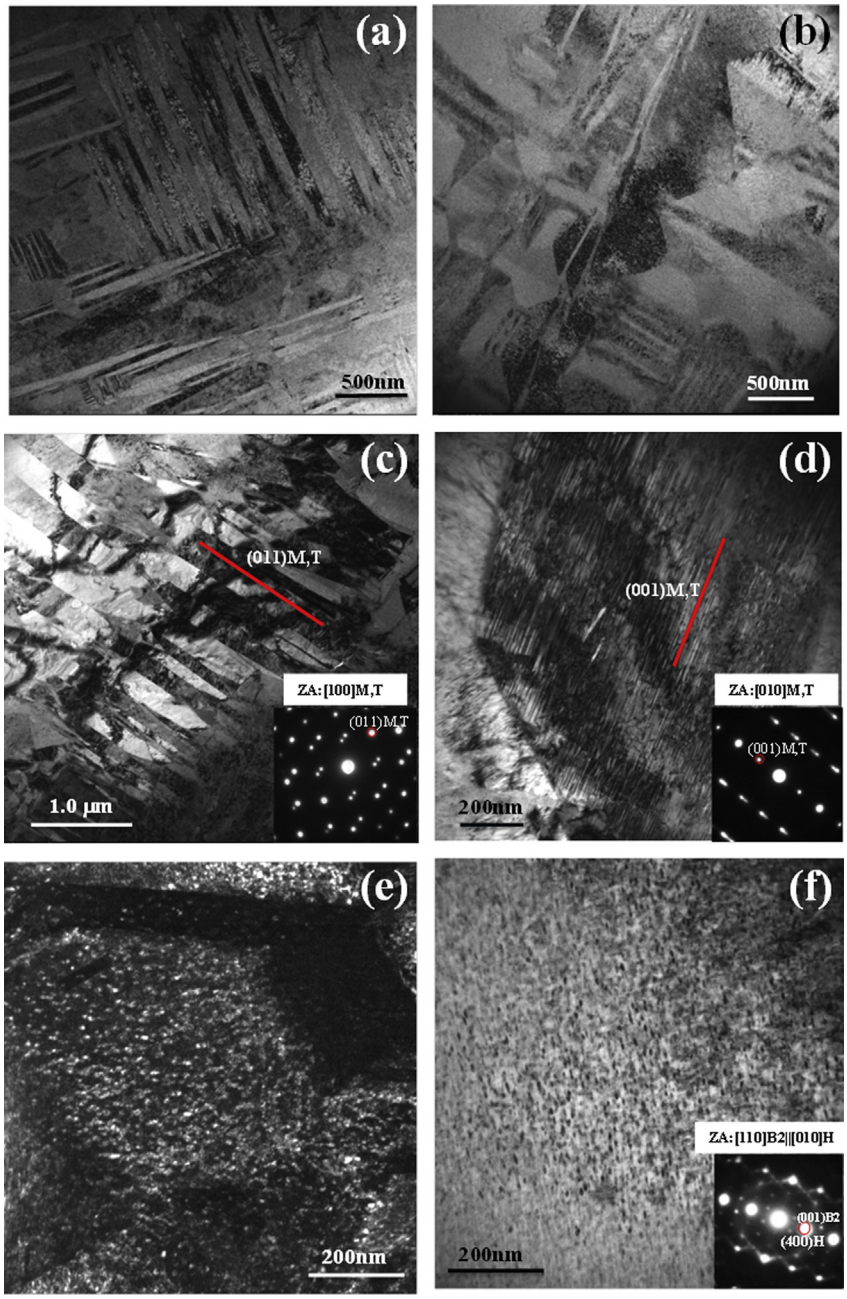

Fig. 3. (a & b) BF-TEM micrographs showing general morphology of the twin variants, (c) analysis of twin variant plates within a set, (d) analysis of twins within a variant plate, (e) dark-field image showing fine precipitate phase, (f) use of electron diffraction for confirmation of the precipitate phase as H-phase. Projection of common planes is marked by red lines in (c & d). (For interpretation of the references to colour in this figure legend, the reader is referred to the web version of this article.)

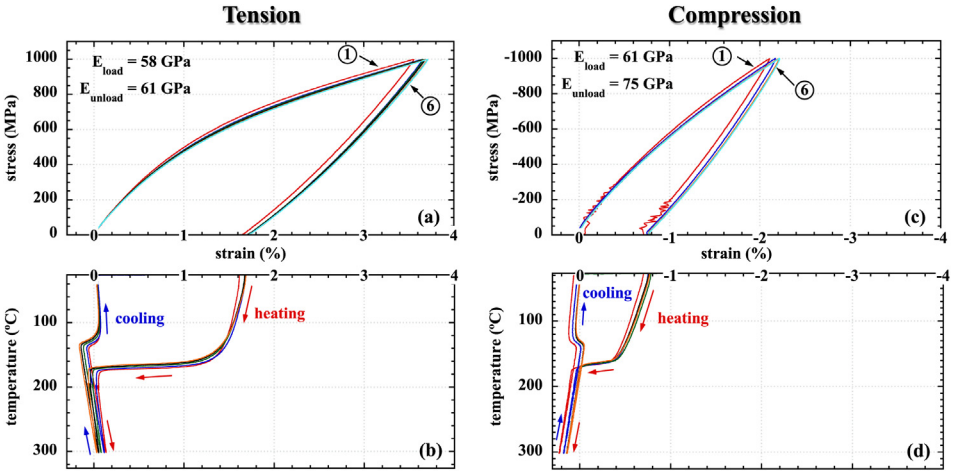

Fig. 4. Stress–strain–temperature curves for the $Ni_{50.3}Ti_{29.7}Hf_{20}$ alloy in uniaxial tension and compression. (a) Tensile stress-strain behavior, and (b) corresponding unconstrained thermal recovery after each tensile deformation in (a), (c) compressive stress–strain behavior, and (d) corresponding unconstrained thermal recovery after each compressive deformation in (c).

control at a rate of 1×10^{-4} s^{-1}. Specimens isothermally deformed and unloaded at room temperature were subsequently (i) re-loaded cyclically to 1 GPa or (ii) heated and cooled once through the phase transformation and re-loaded.

Isobaric testing in compression consisted of thermal cycling between 30 and 300 °C at a constant engineering stress of 0, −100 and −200 MPa for up to 100 cycles and at least 10 thermal cycles at stresses as high as −700 MPa. The loading segment was done at room temperature in load control at a rate of 20 MPa/min. At the end of each series of isobaric strain-temperature tests, specimens were subjected to stress-free thermal cycles to examine the extent of any two-way shape memory effect (TWSME) that may have developed. In this case, TWSME is defined as the ability to change and remember shapes on both heating and cooling without an external biasing force. Additionally, the same specimens were then re-loaded to a different stress level and thermal cycling continued in order to examine the history dependence of the material.

2.4. *In situ* diffraction and thermomechanical testing

In situ synchrotron X-ray diffraction experiments were performed at the High Energy Materials Science (HEMS) beamline at the German high-brilliance synchrotron radiation storage ring PETRA III, at DESY, Hamburg. Compression specimens, 5 mm in diameter and 10 mm in length, were deformed using a BÄHR DIL805 dilatometer with a maximum load capability of 25 kN at temperatures up to 1500 °C [16]. Test specimens were inductively heated using a heating rate of 20 °C/min and cooled by flowing argon gas around the sample environment. Diffraction measurements were performed with 100 keV photon energy ($\lambda = 0.12427$ Å) in transmission geometry. A beam cross section of 500× 500 μm was used with a sample-to-detector distance of 1.572 m. Debye–Scherrer diffraction rings were recorded using a MAR345 image plate detector (345 mm area diameter) with 100 μm pixel size. A schematic of the diffraction setup is shown in Fig. 1.

The *in situ* experiments consisted of load-biased cycling between 30 and 300 °C at constant engineering stresses of 0, −100, −200 MPa, and back to the unloaded condition at 0 MPa. At each stress level (2 cycles each), diffraction data was continuously collected during the heating and cooling cycles, which were run at a rate of 20 °C/min. Data processing was performed using the Fit2D software [17], where spectra were integrated over azimuthal increments of 10° into 36 slices for better grain statistics. Variations in peak intensities and peak positions were obtained by fitting individual diffraction peaks with a pseudo-Voigt function. Lattice strains were calculated from the peak shifts using the change in d-spacing where the initial d-spacing was taken in the nominally unloaded condition. The Rietveld method implemented in the Materials Analysis Using Diffraction (MAUD) software was used for texture analysis [18,19]. This alloy exhibits a B19′ martensite phase at room temperature and a B2 austenite phase at 300 °C, as described in detail in Ref. [7]. Phases were best fitted using a $P112_1/m$ monoclinic space group for B19′ martensite and $Pm\bar{3}m$ cubic

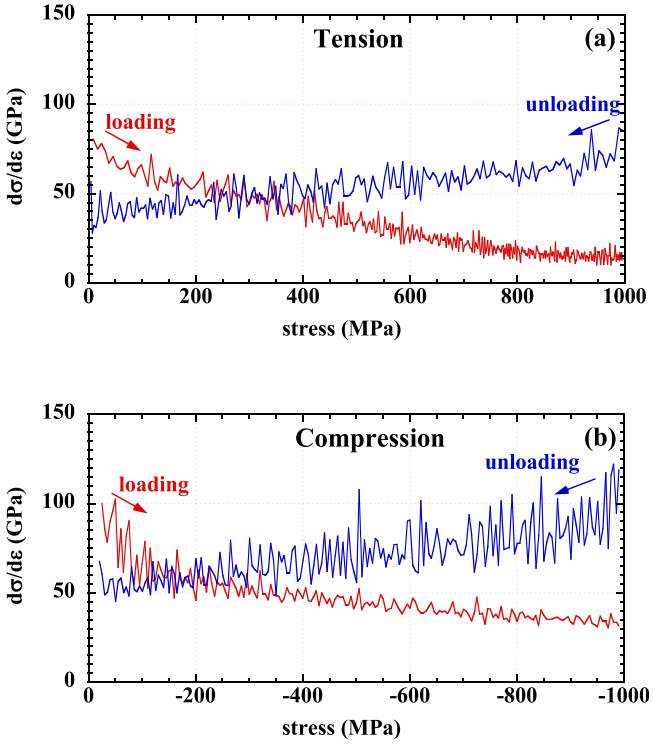

Fig. 5. First derivative of stress with respect to strain ($d\sigma/d\varepsilon$) for (a) tension and (b) compression loading.

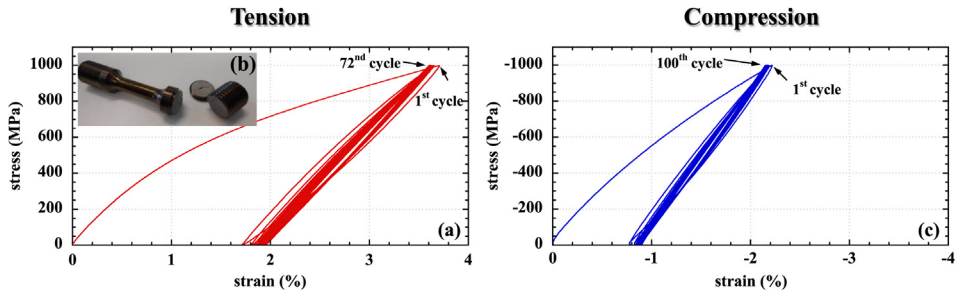

Fig. 6. Room temperature cyclic stress–strain responses of $Ni_{50.3}Ti_{29.7}Hf_{20}$ in (a) tension and (c) compression. The inset (b) indicates the specimen fracture site at the 72nd tensile cycle.

space group for B2 austenite. The best fit lattice parameters were $a = 3.039$, $b = 4.102$, $c = 4.871$ Å, $\alpha = \gamma = 90°$, $\beta = 104.1°$ for monoclinic martensite, and $a = 3.089$ Å for cubic austenite.

3. Results and discussion

3.1. Microstructure – aged material

The microstructure at room temperature was martensitic (B19′) with an average grain size of approximately 40 μm as revealed by optical microscopy (Fig. 2a). Formation of (Hf,Ti)C, as observed in previous versions of this alloy [7–10], was prevented by using a water-cooled copper crucible instead of graphite during melting. However, due to a high affinity of Hf for O_2, formation of HfO_2 particles (size $\leq$ 1 μm) could not be avoided (Fig. 2b–d). In the TEM, a representative martensitic morphology was clearly visible and consisted primarily of two sets of twin variant plates at right angles to each other (Fig. 3a), with small areas of mosaic zig-zag twin structure (Fig. 3b). Each primary set contained variant plates that were related to each other by {011} Type I twins (Fig. 3c). This twinning system has been reported earlier in both Ni-rich [20] and Ti-rich [21] NiTiHf alloys. Within each variant plate fine twins were observed, which were identified as $(001)_{B19'}$ compound twins (Fig. 3d). In addition, the aging treatment produced very fine and highly dense precipitates (size $\leq$ 15 nm) distributed uniformly throughout the matrix (Fig. 3e). Analysis of the selected area diffraction patterns (Fig. 3f), confirmed this phase to be the so called “H-phase” which has been described in detail in recent papers by Yang et al. [14] and Santamarta et al. [6]. The “H-phase” is reported to have a face-centered orthorhombic lattice ($a = 1.264$ nm, $b = 0.882$ nm, $c = 2.608$ nm) with a space group of F 2/d 2/d 2/d (# 70), and a measured composition of $Ni_{52}Ti_{19}Hf_{29}$ (at.%) [14]. It is this fine phase that is responsible for providing the high-strength and stability of the alloy, as described in the remaining sections of this paper.

3.2. Isothermal behavior – tension and compression

The stress–strain–temperature curves for the $Ni_{50.3}Ti_{29.7}Hf_{20}$ alloy in uniaxial tension and compression are shown in Fig. 4. For ease in comparison, the compression curves (Fig. 4c and d) were plotted on the first quadrant to directly observe the tension–compression asymmetry and the corresponding differences in strain magnitudes and ensuing strain recoveries. The testing sequence consisted of (*i*) loading to 1 GPa at room temperature (in either tension or compression), (*ii*) unloading to 0 MPa, (*iii*) heating to 300 °C, and (*iv*) cooling back to room temperature, with the entire sequence repeated for six cycles. For both tensile and compressive loading, room temperature stress-strain responses (Fig. 4a and c) were identical after the first cycle (Fig. 4b and d) and no plastic strain was observed during the initial loading to 1 GPa. The strong tension-compression asymmetry is due to differences in martensitic variant selection (variant reorientation and detwinning) in tension and compression deformation modes as was observed in binary NiTi alloy [22,23]. This deformation strain, 3.7% in tension and 2.2% in compression at 1 GPa stress, is a combination of elastic strain and inelastic martensite variant reorientation/detwinning, but no discernible stress plateau or demarcation between the two mechanisms was observed.

This behavior is further quantified in Fig. 5 by taking the first derivative of stress with respect to strain ($d\sigma/d\varepsilon$). The first derivatives, while a little “noisy”, exhibit a non-zero slope along the entire curve during both loading and unloading, indicating the nonlinear stress–strain response. Since this Ni-rich alloy is a two-phase material containing a fine dispersion of second phase precipitates, an increasing externally applied stress is essential in continuing the reorientation and detwinning process. Thus, a distinct plateau is not observed as in some binary, equiatomic NiTi alloys [24]. In addition, this isothermal deformation did not generate any TWSME, likely due to the absence of permanent plastic deformation. While acknowledging the non-linear loading response, application of a best linear-fit through the initial loading and unloading portions of curves in Fig. 4a and c (approximately

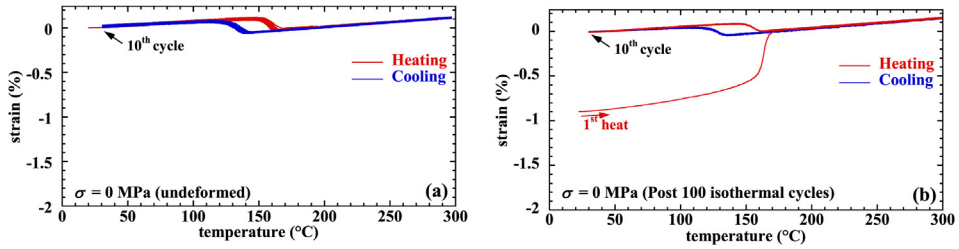

Fig. 7. No-load strain-temperature response for $Ni_{50.3}Ti_{29.7}Hf_{20}$ showing ten thermal cycles (at 0 MPa) for (a) an undeformed ‘virgin’ sample and (b) after deformation according to Fig. 4b.

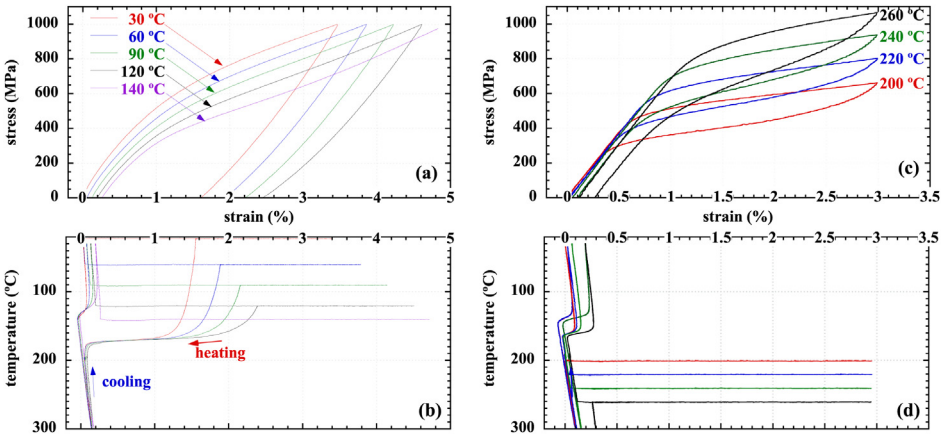

Fig. 8. Stress–strain–temperature curves for the $Ni_{50.3}Ti_{29.7}Hf_{20}$ alloy in uniaxial tension at different temperatures. (a) Stress–strain behavior below A_s, and (b) corresponding unconstrained thermal recovery after each deformation sequence in (a) and, (c) stress-strain behavior above A_f, and (d) corresponding unconstrained thermal recovery after each deformation sequence in (c).

through 100 MPa), results in an estimated range for the "apparent" Young's modulus of 58–61 GPa in tension, and 61–75 GPa in compression over the initial loading and unloading sections of the stress–strain curves.

Cyclic isothermal tests were also conducted at room temperature in tension and compression as shown in Fig. 6. Specimens were cyclically loaded to 1 GPa and unloaded (repeated for a maximum of 100 cycles) to examine strain ratcheting and instabilities if any. Two specimens were tested in tension and both of them failed at the threads, the first one during the 72nd cycle and the second one during the 85th cycle. Cyclic stress–strain data in tension for the sample that failed at 72 cycles is shown in Fig. 6a. An image of the actual test sample that fractured is shown in Fig. 6b. It should be noted that no localized deformation or necking was observed in the samples' gage sections, and failure occurred due to defects introduced during thread machining operations at the high stress concentration located at the thread roots. On the other hand, samples tested in compression (using the same geometry), did not fracture during testing to the 100 cycle limit used in this investigation. The cyclic compression stress–strain response is shown in Fig. 6c.

Irrespective of the testing mode, the strain evolution exhibited similar behavior, i.e., the strain at the loaded condition (±1 GPa) shifted $^{T}0.1$ and $^{C}0.08\%$ towards zero with cycling, and the strain values at 0 MPa shifted $^{T}0.23$ and $^{C}0.12\%$ towards higher strain with cycling, where superscripts 'T' and 'C' refer to testing performed in tension and compression, respectively. If the sample is then heated through the transformation (only to 300 °C) and the reoriented martensite is recovered and then the sample is deformed again at room temperature, the stress–strain curve will once again look like the initial cycle 1 loading curve and not retain the stiffer slope exhibited at the higher cycles. Thus, this indicates that the stress–strain slopes become steeper with increasing number of cycles, due to stabilization of the favored martensite variants. In addition, aside from these small strain shifts, the cyclic loops were repeatable with no accumulation of plastic strain. Post thermal cycling at 0 MPa of the undeformed and the isothermally cycled compression samples (Fig. 7a and b, respectively) showed no difference in strain–

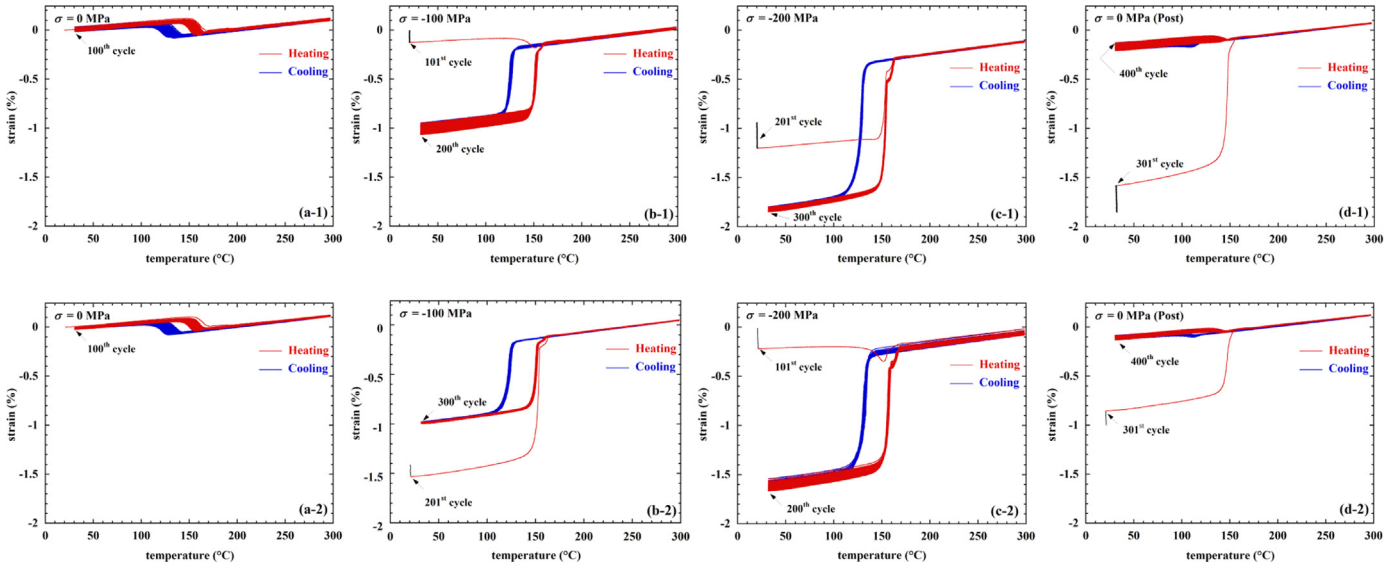

Fig. 9. Isobaric strain–temperature response of the $Ni_{50.3}Ti_{29.7}Hf_{20}$ for different loading histories, i.e., a-1 thru d-1 and a-2 thru d-2. The constant stress level and cycle number are indicated for each set of curves.

temperature response compared to the initial starting material. Further, this no-load thermal cycling was extended up to 100 cycles (not shown in Fig. 7b) and no TWSME or any other change in behavior was observed; the material performing similar to an undeformed 'virgin' material with no prior history (Fig. 7a).

Additional isothermal tests at temperatures between 30 and 260 °C were conducted to assess the effect of temperature on the mechanical response and stress-induced transformation behavior of this material. The results for tensile loading are shown in Fig. 8. These tests were performed in series, where after each load-unload cycle (Fig. 8a and c) samples were heated and cooled once through the phase transformation at 0 MPa (Fig. 8b and d), before heating to the next test temperature and re-loading. Below the A_s temperature (Fig. 8a and b), the stress–strain curves exhibited a lower

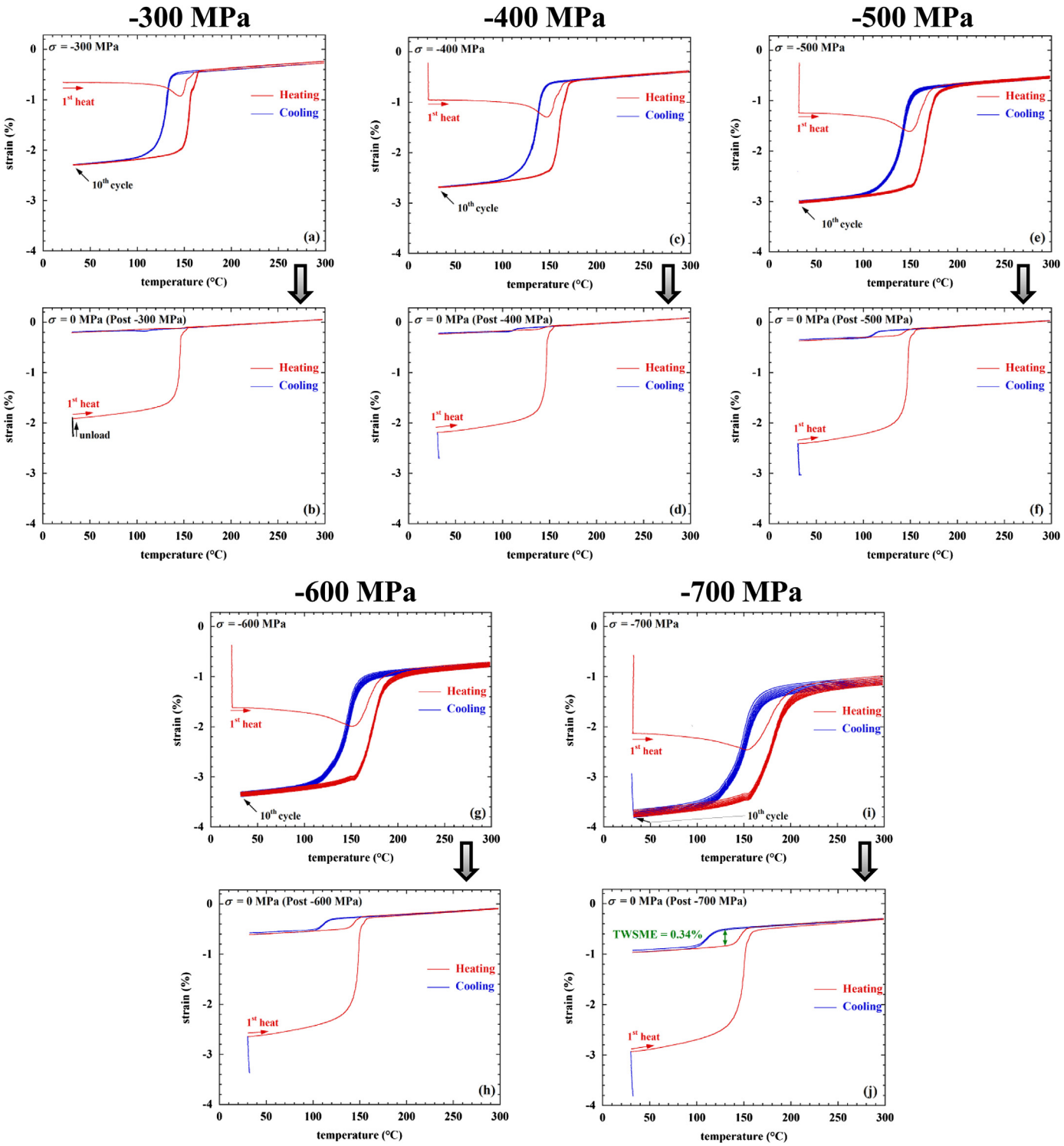

Fig. 10. Isobaric strain–temperature response of the $Ni_{50.3}Ti_{29.7}Hf_{20}$ alloy at different stresses. After each set of ten isobaric thermal cycles at constant stress, an additional ten stress-free thermal cycles were applied before increasing to the next load.

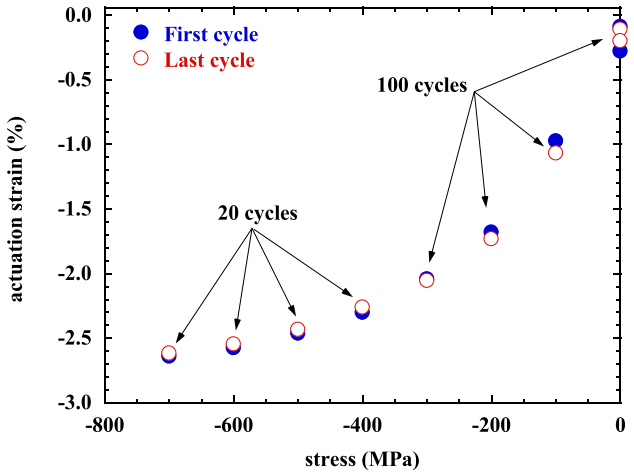

Fig. 11. Compressive actuation strain as a function of stress for the $Ni_{50.3}Ti_{29.7}Hf_{20}$ alloy for the first cycle (solid symbols), and for the last cycle (10th) (open symbols).

hardening rate with increasing temperature (Fig. 8a) and accumulation of a small although permanent deformation of ~0.2% total unrecovered strain after five load-unload cycles at temperatures between 30 and 140 °C. It should be noted that the amount of permanent strain that accumulated each cycle tended to increase as the temperature increased, although the total strain accumulation was small.

Above the A_f temperature (Fig. 8c and d), the stress–strain curves exhibited an initial linear elastic loading of the austenite phase followed by a stress plateau associated with the stress-induced martensitic (SIM) transformation. Note that while the curves in Fig. 8a were limited to 1 GPa, the curves in Fig. 8c were limited to 3% strain, since the primary interest was in the superelastic response in this case. The unrecovered strains were less than 0.02% (almost negligible) for samples deformed at 200 and 220 °C, 0.08% at 240 °C and 0.18% at 260 °C. The onset stress for the SIM estimated using the 0.2% offset stress criterion, increased with increasing test temperature consistent with a Clausius–Clapeyron relationship. The average elastic moduli for the austenite phase measured above A_f were 75 GPa in tension (from Fig. 8c) and 80 GPa in compression (curves not shown).

A small TWSME was introduced, illustrated in Fig. 8b and d, as the material started to accumulate unrecovered strains. Loading

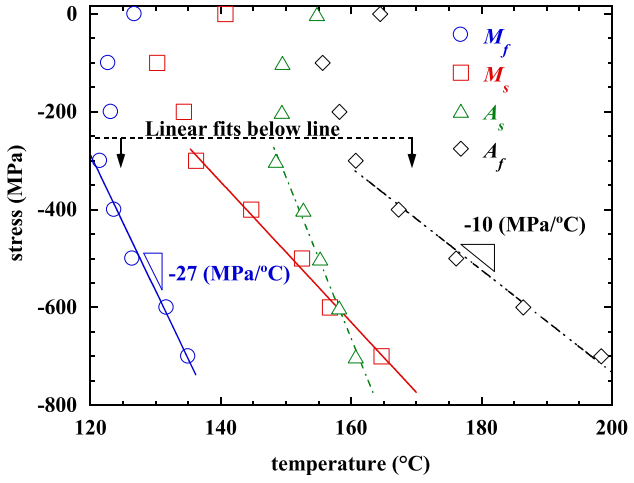

Fig. 12. Transformation temperatures for the $Ni_{50.3}Ti_{29.7}Hf_{20}$ alloy as function of compressive stress.

below A_s or above A_f, where the deformation was not fully reversible (e.g., 140 or 260 °C test temperatures), is expected to result in internal stress fields that can be caused by a number of sources including dislocation arrays. However, the magnitude of the TWSME was less than 0.2% when initiated through isothermal deformation, which is an order of magnitude less than that observed in binary NiTi under comparable conditions [24].

3.3. Isobaric behavior–compression

Isobaric thermal cycles in compression are shown in Fig. 9. For all testing, an upper cycle temperature of 300 °C (130 °C above A_f) was used to ensure complete phase transformation under load. Two cases were considered to examine the history dependence of this alloy: the first case (labeled a-1 through d-1) consisted of series thermal cycling under 0 MPa, −100 MPa, −200 MPa, and back to 0 MPa in this sequence. The second case (labeled a-2 through d-2) consisted of series thermal cycling of a new sample under 0 MPa, −200 MPa, −100 MPa, and back to 0 MPa, noting that the second and third loading sequence was reversed in the second case as compared to that in the first case. At each stress level, 100 cycles were performed to enhance any effects due to thermomechanical cycling, with a total of 400 cycles on each specimen.

From the stress-free strain–temperature response, the martensite and austenite coefficients of thermal expansion (CTE) were measured to be 7×10^{-6}/°C and 11×10^{-6}/°C, respectively. The transformation strain of 0.17% associated with the undeformed sample [Fig. 9(a-1)] is assumed to be due to the combined Bain strain and lattice invariant shear.

On loading to −100 MPa [Fig. 9 (b-1)], a characteristic transient response was observed on the first heating cycle, followed by development of a larger induced strain on cooling under load. Subsequent cycles were all very similar with a minor exception. With the accumulation of cycles, the end-strain in the austenite phase remained nearly constant over the 100 cycles, while the end-strain in the martensite evolved to slightly higher values as more detwinning/reorientation of the martensite phase occurred. This evolution resulted in a growing actuation strain, determined by taking the difference between the martensite and austenite true end-strains. Note that when referring to the transformation strain as opposed to actuation strain, the former is determined as the relative true strain between the austenite finish and austenite start intersections as demonstrated in Ref. [1], which in this case also follows the same trend as the actuation strain. In either case, the total increase in strain over 100 cycles was relatively minor, less than 0.16%.

At the end of thermal cycling at −100 MPa stress, the compressive stress was increased to −200 MPa [Fig. 9 (c-1)], and an additional 100 thermomechanical cycles followed. Similar behavior can be observed with regard to the first transient heating curve and the evolution of the martensite end-strain, although much smaller evolution than the previous stress value was attained. The specimen was then unloaded to 0 MPa and thermally cycled [Fig. 9 (d-1)], where all the strains that were generated throughout the isobaric cycling were recovered on the first heating cycle. The end-strain in the austenite phase was identical to the initial 0 MPa thermal cycle [Fig. 9 (a-1)], but the end-strains in the martensite exhibited a different behavior displaying a narrower transformation loop. Nonetheless, there was no TWSME developed at the end of cycling in this scenario.

Similar observations were made from the second case shown in Fig. 9 (a-2) through 9 (d-2). In this case, the −200 MPa stress was applied first [Fig. 9 (c-2)] before the −100 MPa stress. The results in Fig. 9 (c-2) indicate that strain ratcheting is taking place at both phases, but higher evolution occurs in the martensite phase (0.17%)

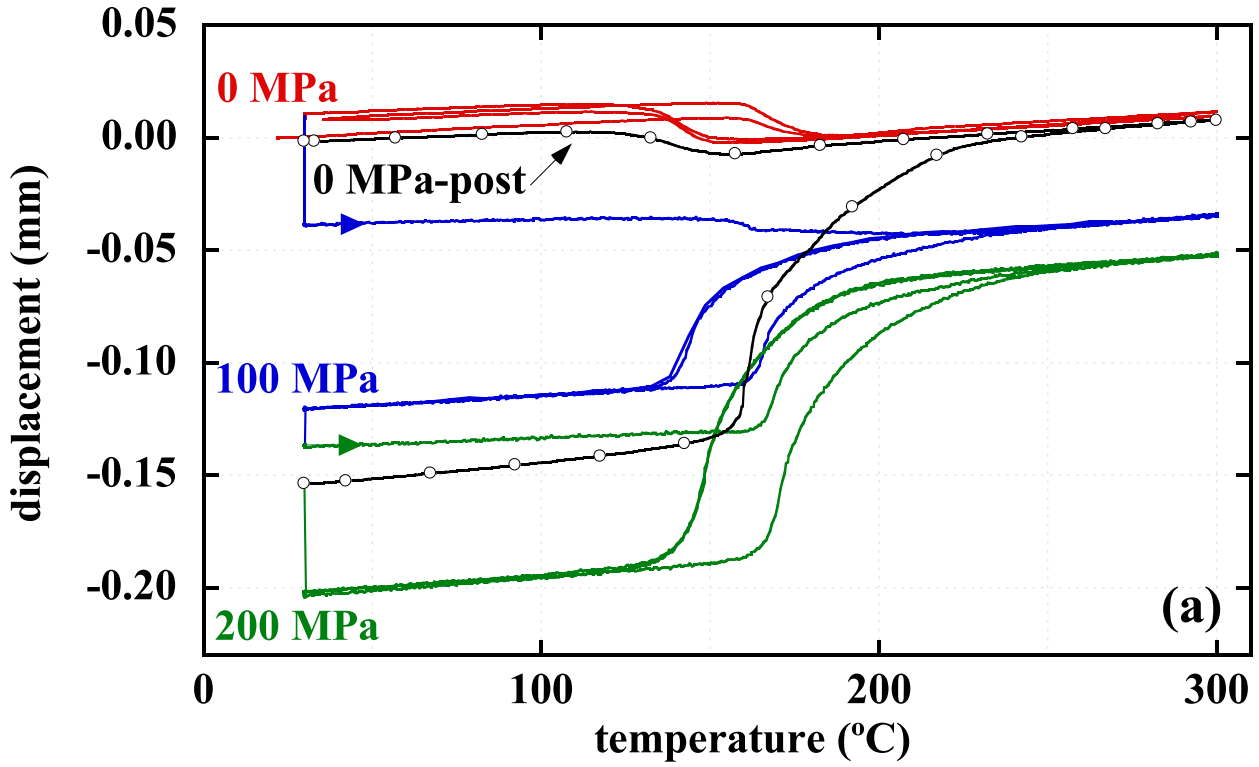

Fig. 13. *In situ* isobaric displacement-temperature response of the $Ni_{50.3}Ti_{29.7}Hf_{20}$ alloy at different stresses.

versus the austenite phase (0.09%). Once the stress was reduced to −100 MPa, the thermomechanical response was stable without any evolution, though all SME values were similar to those shown in Fig. 9 (b-1). Overall, comparing the two cases, the strain-temperature responses show similar behavior indicating that except for stabilization in the evolutionary behavior at −100 MPa the shape memory response is essentially history independent under this range of stresses due to insignificant levels of permanent or plastic deformation. Furthermore, there was no TWSME present after cycling with the current load and temperature conditions in either case, which is also consistent with the lack of permanent deformation during thermomechanical cycling.

Additional isobaric tests were performed at higher stresses followed by stress free thermal cycles (Fig. 10). At each stress level, the sample was thermomechanically cycled ten times, followed by ten stress-free thermal cycles. Then the same sample was reloaded to the next stress level and cycled again. Strain evolution (strain ratcheting at both phases), while very small in all cases, was noticeable starting at stresses of −500 MPa and higher, and at those stresses, the TWSME started to appear and grow with higher loads as indicated in Fig. 10. In this testing configuration, a maximum TWSME of 0.34% was obtained post cycling to −700 MPa. This is attributed to plastic deformation, most likely in the austenite phase, and the possibility of retained martensite as was observed in binary NiTi [25] and NiTiPd alloys [26]. However, relatively speaking, the load stability of this alloy is highly remarkable, since the strain evolution is over an order of magnitude less at stress levels twice as high as observed in other shape memory alloys [25,26]. In addition, a significantly reduced TWSME due to thermomechanical cycling was observed compared to that developed in other NiTi-based systems at a fraction of the "training" stress [27]. This can be either a positive or negative attribute depending on the desirability of TWSME in a given application.

A summary of the actuation strain as a function of stress is shown in Fig. 11. Both the actuation strains on the first and last cycle (100 cycles for 0 to −300 MPa, 20 cycles for −400 to −700 MPa) are plotted for comparison. It was found that only a small variation from the first to the last cycle was obtained, and the actuation strain appeared to reach a limit at a maximum of 2.65% in compression.

The stress dependence of the transformation temperatures is shown in Fig. 12. From 0 to −200 MPa, the temperatures follow a non-linear behavior with an initial shift towards lower temperatures followed by near constant behavior as the stress increases. At stresses higher than −200 MPa, the transformation temperatures follow an expected linear trend and shift to higher temperatures with increasing stress. Linear correlations were fit through the stress-temperature data at stresses higher than −200 MPa as shown in Fig. 12. It should be noted that the stress–temperature data of Fig. 12 can also be fitted with a parabolic relationship to capture the entire behavior. In either case, the data presented is an actual material response and should be used in the appropriate form when used in design or SMA model calibration.

3.4. *In situ* synchrotron X-ray diffraction results

Analogous to the isobaric *ex situ* testing presented above, *in situ* testing was conducted to mimic the loading sequence of the first case in Fig. 9, but for only 2 cycles at each load step. The corresponding displacement-temperature response is presented in Fig. 13. After two cycles at 0, −100 and −200 MPa, successively, the sample was unloaded to 0 MPa and heated once through the phase transformation where all the strains were recovered. Diffraction spectra corresponding to the second cycle of each load step of Fig. 13 are shown in Fig. 14 as the sample undergoes the phase transformation from martensite to austenite during heating. These patterns were obtained by integrating the full diffraction ring over the azimuthal angle (ψ) defined in Fig. 1. Existing phases were

previously identified [7] as B2 austenite at high temperature and B19′ martensite at lower temperature. The results indicate complete transformation with thermal cycling under all conditions shown in Fig. 13. There is no evidence of retained martensite above the bulk A_f, even under an isobaric stress of −200 MPa. In contrast, residual martensite is noted in binary NiTi even when cycling under stress free conditions [28]. In addition, there is no indication of residual austenite below the measured M_f temperature. The transformation is complete in both directions at the representative martensite and austenite finish temperatures.

Normalized intensities (I/I_0) of select martensite peaks at room temperature and austenite peaks at 300 °C were determined as a function of the azimuthal angle integrated over 10° ψ segments, where $\psi = 0°$ is the compression axis. Intensity data was plotted in normalized scale to compare the intensity changes with cycling and changing macroscopic stresses. Fig. 15 contains several martensite peaks at room temperature plotted on radial 10° ψ segments for various stresses. The intensities of some of the martensite planes, particularly along the loading direction, varies as the sample was cycled under load, indicative of the formation and reorientation of preferred martensite variants capable of accommodating the applied strain that takes place on constrained cooling. The intensities further change from −100 to −200 MPa, which is macroscopically manifested by additional transformation strains as

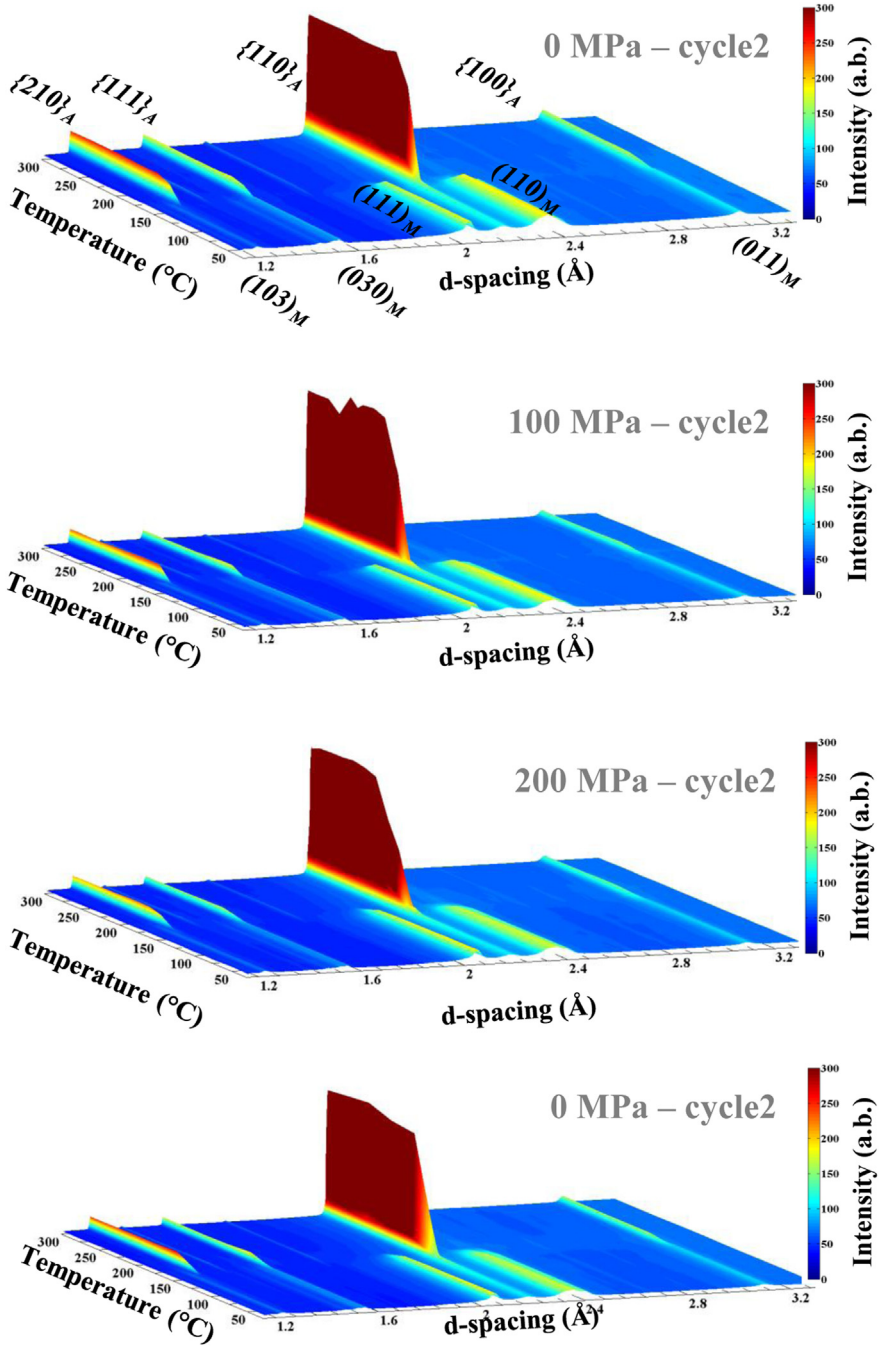

Fig. 14. *In situ* synchrotron X-ray diffraction spectra corresponding to the second heating cycle of each load step of Fig. 13. These spectra show the martensite to austenite transition on heating.

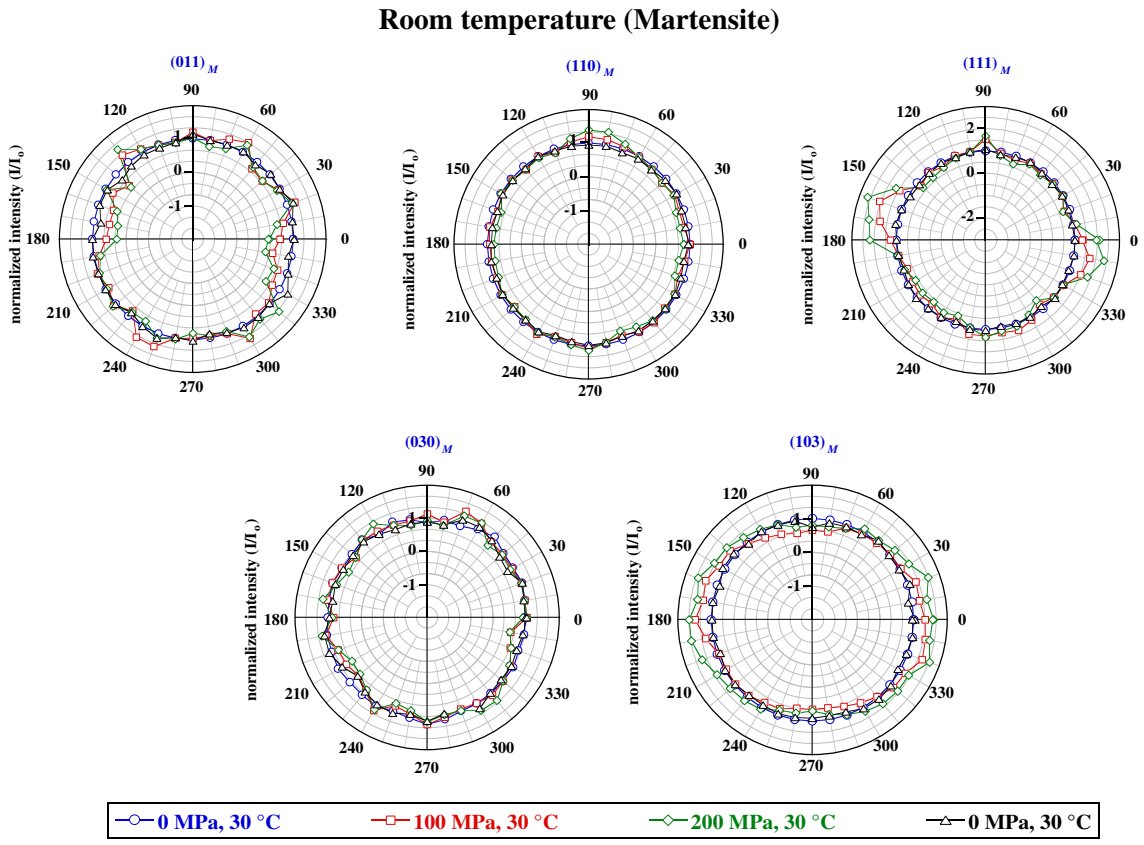

Fig. 15. Normalized diffraction intensities (I/I_0) of select martensite peaks at room temperature as a function of the azimuthal angle integrated over 10° ψ segments, where $\psi = 0°$ is the compression axis.

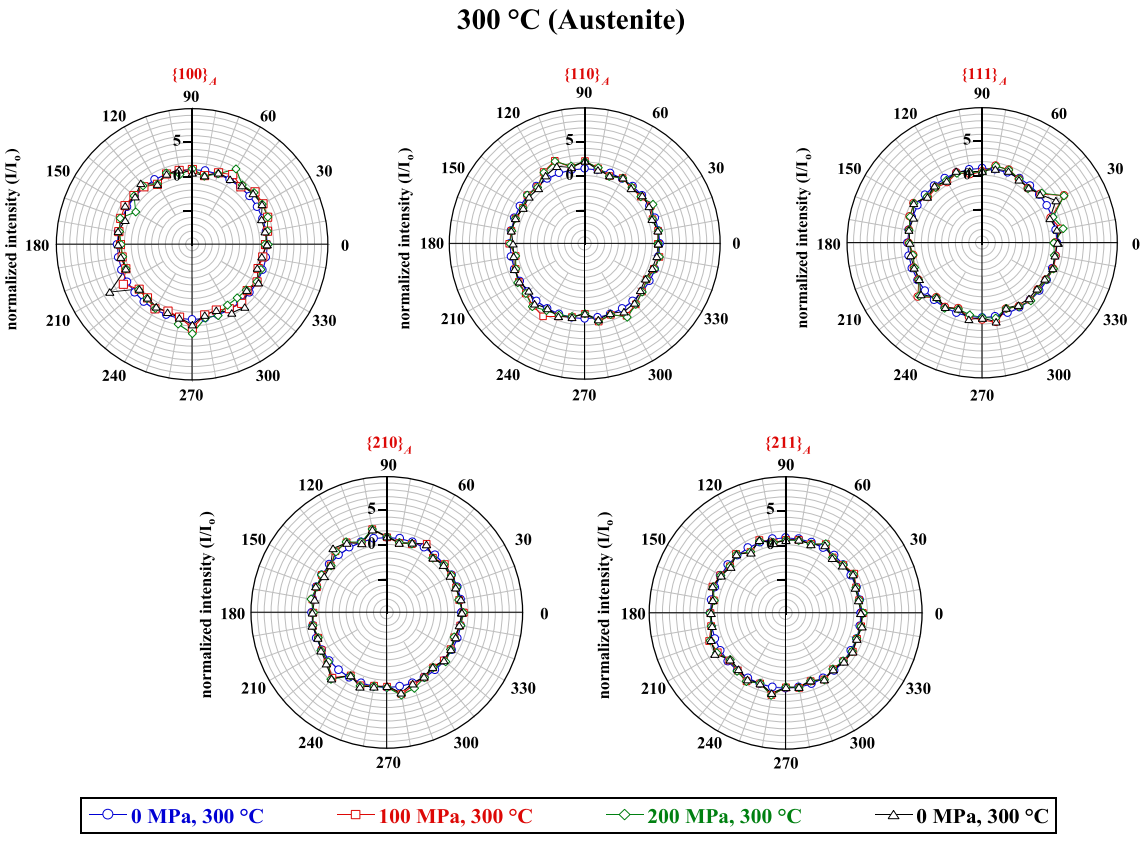

Fig. 16. Normalized diffraction intensities (I/I_0) of select austenite peaks at 300 °C as a function of the azimuthal angle integrated over 10° ψ segments, where $\psi = 0°$ is the compression axis.

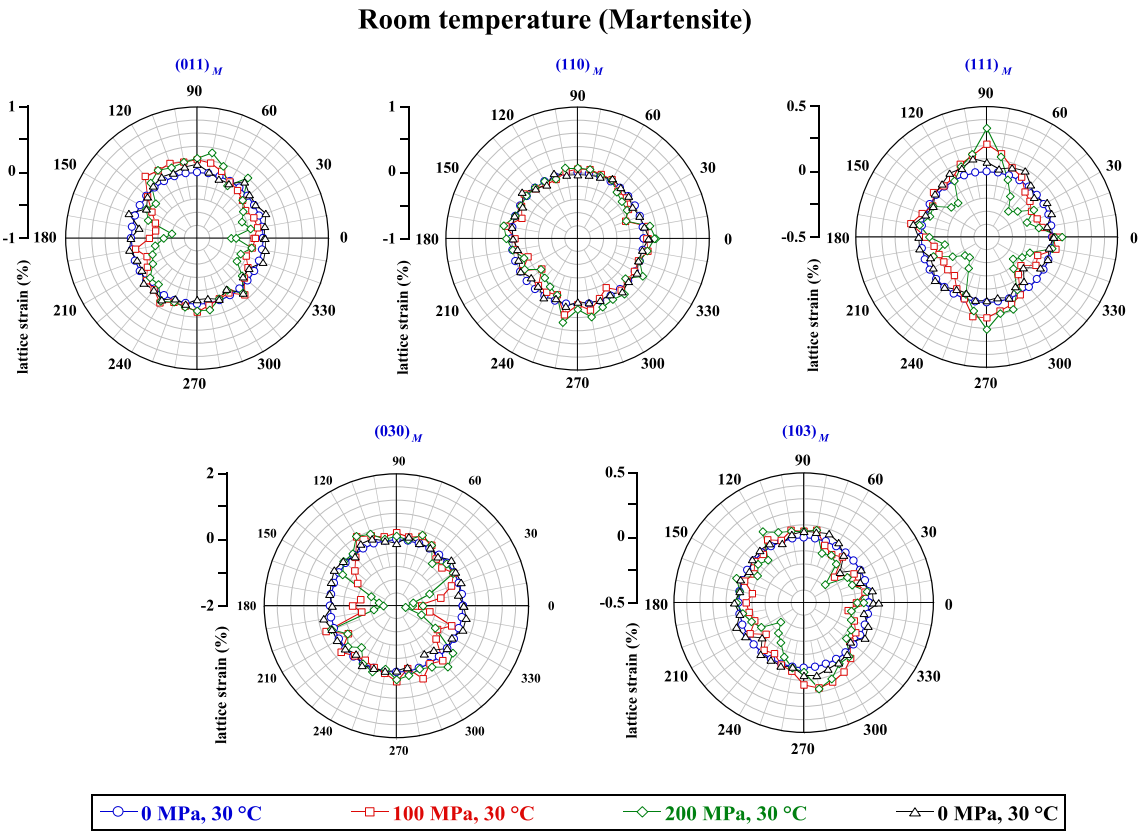

Fig. 17. Lattice strains for a select family of planes in the martensite phase at room temperature as a function of the azimuthal angle integrated over 10° ψ segments.

shown in Figs. 9 and 14. Microstructurally, the $(011)_M$, $(111)_M$ and $(103)_M$ lattice planes preferentially orient with the loading axis, while the $(110)_M$ and $(030)_M$ planes display only a slight variation in intensity. Once the load was removed, the intensities of the individual lattice planes return to their initial pre-cycling values at 0 MPa, consistent with the fully reversible macroscopic observations. The diffraction data of Fig. 15 served to provide direct evidence of isobaric martensite reorientation of preferred variants in order to accommodate the applied macroscopic strain without permanent deformation. Although the load was limited at 200 MPa, the varying texture with increasing load indicates the additional transformation strain capability of this alloy as macroscopically shown in Fig. 11.

In a similar analysis, the normalized intensities of B2 austenite at 300 °C are shown in Fig. 16 for various stresses. As opposed to the changing intensities of the martensite phase, the austenite intensities did not vary with cycling or with changing load. This unchanging austenitic texture is also an indication that no new or additional deformation mechanisms occur in the austenite phase due to thermal cycling under the current conditions and that the underlying microstructure has not been affected by prior history. These microstructural results are fully consistent with the lack of plastic deformation evident in the mechanical test data under the current conditions and help explain why the strains generated during the isobaric thermal cycling were fully reversible.

Lattice strains for a select family of planes were calculated using $\varepsilon_{hkl} = \Delta d/d_0$, where d_0 is the initial d-spacing of the starting material at 0 MPa macroscopic stress. Lattice strains in the martensite phase, shown in Fig. 17, exhibited an anisotropy associated with the low symmetry monoclinic phase. At $\psi = 0$, which corresponds to the loading axis, some lattice planes exhibited strains as high as −1.6% in the case of the $(030)_M$ planes, while others developed an order of magnitude less strain such as the $(110)_M$ planes. Moreover, there is large deviation in strain magnitude over different azimuthal angles as illustrated by the $(111)_M$ planes. Regardless of the initial anisotropy or strain heterogeneity, all the lattice strains were recovered after load removal consistent with the macroscopic findings presented in previous sections.

In contrast to the martensite phase, lattice strains for the austenite phase are mostly isotropic in nature as shown in Fig. 18. Within the measurements error, the B2 lattice planes exhibit similar strain behavior and magnitude (compressive along $\psi = 0$, tensile along $\psi = 90$) indicating the isotropy associated with the parent phase. Nevertheless, similar observations were made regarding the strain reversibility after load removal with no residual lattice strain observed. The lattice strain reversibility is also an indication of the lack of internal/residual strains that would otherwise help drive the TWSME. Without any internal stresses, the material, as demonstrated macroscopically, exhibited no TWSME under the test conditions shown in Fig 14.

4. Conclusions

Basic mechanical, thermomechanical, and microstructural behaviors of the precipitation strengthened, Ni-rich $Ni_{50.3}Ti_{29.7}Hf_{20}$ high temperature shape memory alloy were investigated under isothermal and isobaric conditions. Based on the *ex situ* macroscopic and *in situ* synchrotron X-ray diffraction results, the following conclusions can be made:

1. Isothermal deformation of the martensite phase at room temperature resulted in no plastic deformation or other irrecoverable strains when tested to 1 GPa uniaxial tensile and

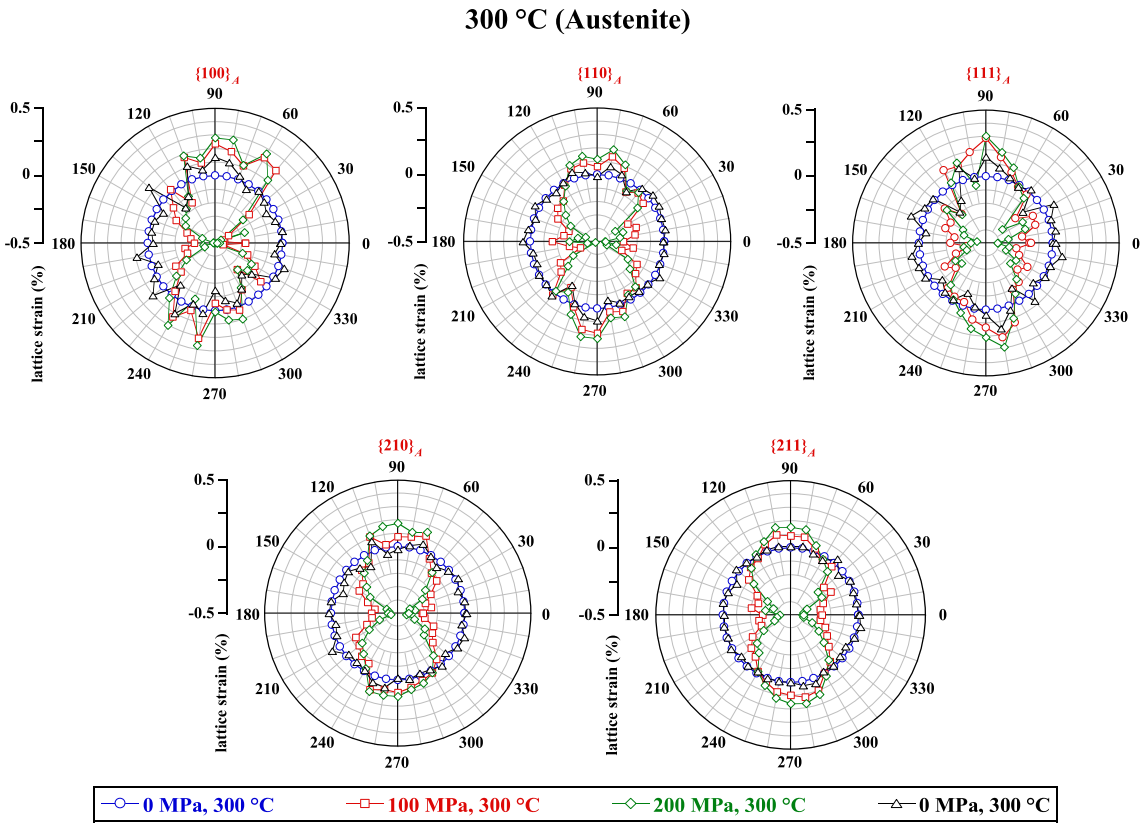

Fig. 18. Lattice strains for a select family of planes in the austenite phase at 300 °C as a function of the azimuthal angle integrated over 10° ψ segments.

compressive stresses. In addition, extended cycling at this stress level did not introduce any permanent deformation and all strains were transformation related and recovered upon heating through the phase transformation.

2. A near-perfect superelastic behavior, without generation of significant residual strain, was obtained at temperatures between 180 and 220 °C, with recoverable strains on the order of 3% upon unloading. Plastic deformation was apparent only at temperatures higher than 220 °C, resulting in a small ~0.2% TWSME.
3. Isothermal deformation in either the martensite or austenite phases did not yield a large and stable TWSME, mainly due to lack of internal/residual stress fields, since plastic deformation was not introduced under the test conditions investigated.
4. *In situ* diffraction data showed a complete phase transformation between the B19′ and B2 phases with no evidence of retained martensite above A_f, in both the unloaded and loaded conditions. Similarly, there was no indication of residual austenite below the measured M_f temperature.
5. Dimensionally stable responses were observed during isobaric thermal cycling, with no prior training requirement. Stability was also observed in the microstructure. *In situ* diffraction spectra, collected during isobaric thermal cycling, revealed preferentially oriented martensite variants that revert back to the original microstructure upon load removal. No texture changes were observed in the austenite phase and no evidence for plastic deformation was detected in the spectra when cycling with stresses up to −200 MPa. Similarly, measured lattice strains were found to fully recover after load removal and stress-free thermal cycling, leaving no residual strains. These findings are consistent with the lack of macroscopic residual strains and the absence of TWSME.
6. Isobaric thermal cycling at high stresses, exceeding −500 MPa, resulted in slight dimensional instabilities and a maximum TWSME of 0.34% after cycling at −700 MPa. Isobarically, a higher TWSME was obtained compared to the introduction of isothermal deformation, but neither case produced significant TWSME in this alloy.
7. The maximum actuation strain in compression seemed to saturate at approximately 2.65%.

Acknowledgments

Funding from the NASA Fundamental Aeronautics Program, Aeronautical Sciences Project is gratefully acknowledged. Grant NNX08AB51A to UCF is gratefully acknowledged. The authors thank A. Stark for technical support with the diffraction experiments. This work has greatly benefited from the use of the HEMS beamline at the German high-brilliance synchrotron radiation storage ring PETRA III on DESY.

References

[1] Bigelow GS, Padula II SA, Garg A, Gaydosh D, Noebe RD. Characterization of ternary NiTiPd high-temperature shape-memory alloys under load-biased Thermal cycling. Metall Mater Trans A 2010;41:3065–79.
[2] Atli KC, Karaman I, Noebe RD, Garg A, Chumlyakov YI, Kireeva IV. Improvement in the shape memory response of $Ti_{50.5}Ni_{24.5}Pd_{25}$ high temperature shape memory alloy with scandium microalloying. Metall Mater Trans A 2010;41A:2485–97.
[3] Kovarik L, Yang F, Garg A, Diercks D, Kaufman M, Noebe RD, et al. Structural analysis of a new precipitate phase in high-temperature TiNiPt shape memory alloys. Acta Mater 2010;58:4660–73.
[4] Noebe R, Draper S, Gaydosh D, Garg A, Lerch B, Penney N, et al. Effect of thermomechanical processing on the microstructure, properties, and work behavior of a $Ti_{50.5}Ni_{29.5}Pt_{20}$ high-temperature shape memory alloy. In: SMST

2006: proceedings of the international conference on shape memory and superelastic technologies, Pacific Grove, CA; 2008. pp. 409–26.
[5] Evirgen A, Karaman I, Noebe RD, Santamarta R, Pons J. Effect of precipitation on the microstructure and the shape memory response of the $Ni_{50.3}Ti_{29.7}Zr_{20}$ high temperature shape memory alloy. Scr Mater 2013;69:354–7.
[6] Santamarta R, Arróyave R, Pons J, Evirgen A, Karaman I, Karaca HE, et al. TEM study of structural and microstructural characteristics of a precipitate phase in Ni-rich Ni–Ti–Hf and Ni–Ti–Zr shape memory alloys. Acta Mater 2013;61:6191–206.
[7] Benafan O, Noebe RD, Padula II SA, Vaidyanathan R. Microstructural response during isothermal and isobaric loading of a precipitation-strengthened Ni-29.7Ti-20Hf high-temperature shape memory Alloy. Metall Mater Trans A 2012;43A:4539–52.
[8] Coughlin DR, Phillips PJ, Bigelow GS, Garg A, Noebe RD, Mills MJ. Characterization of the microstructure and mechanical properties of a 50.3Ni–29.7Ti–20Hf shape memory alloy. Scr Mater 2012;67:112–5.
[9] Karaca HE, Saghaian SM, Basaran B, Bigelow GS, Noebe RD, Chumlyakov YI. Compressive response of nickel-rich NiTiHf high-temperature shape memory single crystals along the [1 1 1] orientation. Scr Mater 2011;65:577–80.
[10] Bigelow GS, Garg A, Padula III SA, Gaydosh DJ, Noebe RD. Load-biased shape-memory and superelastic properties of a precipitation strengthened high-temperature $Ni_{50.3}Ti_{29.7}Hf_{20}$ alloy. Scr Mater 2011;64:725–8.
[11] Meng XL, Cai W, Chen F, Zhao LC. Effect of aging on martensitic transformation and microstructure in Ni-rich TiNiHf shape memory alloy. Scr Mater 2006;54:1599–604.
[12] Meng XL, Cai W, Fu YD, Li QF, Zhang JX, Zhao LC. Shape-memory behaviors in an aged Ni-rich TiNiHf high temperature shape-memory alloy. Intermetallics 2008;16:698–705.
[13] Ma J, Karaman I, Noebe RD. High temperature shape memory alloys. Int Mater Rev 2010;55:257–315.
[14] Yang F, Coughlin DR, Phillips PJ, Yang L, Devaraj A, Kovarik L, et al. Structure analysis of a precipitate phase in an Ni-rich high-temperature NiTiHf shape memory alloy. Acta Mater 2013;61:3335–46.
[15] Moshref-Javadi M, Seyedein SH, Salehi MT, Aboutalebi MR. Age-induced multi-stage transformation in a Ni-rich NiTiHf alloy. Acta Mater 2013;61:2583–94.
[16] http://thermophysical.tainstruments.com/instruments/dilatometers/dil-805ad-quenching-and-deformation-dilatometer/ 2013.
[17] Hammersley AP. ESRF internal report, ESRF98HA01T, FIT 2D V9.129 reference manual V3.1; 1998.
[18] Lutterotti L, Matthies S, Wenk H-R, Schultz AJ, Richardson JW. Texture and structure analysis of deformed limestone from neutron diffraction spectra. J Appl Phys 1997;81:594–600.
[19] Ischia G, Wenk H-R, Lutterotti L, Berberich F. Quantitative Rietveld texture analysis of zirconium from single synchrotron diffraction images. J Appl Cryst 2005;38:377–80.
[20] Garg A, Bigelow G, Saghaian S, Chumlyakov Y, Karaca H, Noebe RD. Martensitic transformation in a high-temperature high-strength <001> single Crystal NiTiHf shape memory Alloy. In: Proc. IMC-17, International Microscopy Congress (IMC17); 2010. Paper M8.46, Rio de Janeiro, Brazil.
[21] Han XD, Zou WH, Wang R, Zhang Z, Yang DZ. Structure and substructure of martensite in a $Ti_{36.5}Ni_{48.5}Hf_{15}$ high temperature shape memory alloy. Acta Mater 1996;44:3711–21.
[22] Qiu S, Clausen B, Padula II SA, Noebe RD, Vaidyanathan R. On elastic moduli and elastic anisotropy in polycrystalline martensitic NiTi. Acta Mater 2011;59:5055–66.
[23] Stebner AP, Vogel SC, Noebe RD, Sisneros T, Clausen B, Brown DW, et al. Micromechanical quantification of elastic, twinning, and slip strain partitioning exhibited by polycrystalline, monoclinic nickel-titanium during large uniaxial deformations measured via in-situ neutron diffraction. J Mech Phys Solid 2013;61:2302–30.
[24] Benafan O, Padula II SA, Noebe RD, Sisneros TA, Vaidyanathan R. Role of B19' martensite deformation in stabilizing two-way shape memory behavior in NiTi. J Appl Phys 2012;112:093510.
[25] Padula SA, Qiu S, Gaydosh DJ, Noebe R, Bigelow Glen, Garg A, et al. Effect of upper-cycle temperature on the load-biased, strain-temperature response of NiTi. Metall Mater Trans A 2011;43:4610–21.
[26] S. Qiu. Ph.D. dissertation. University of Central Florida, Orlando, FL; 2010.
[27] Atli KC, Karaman I, Noebe RD, Gaydosh D. The effect of training on two-way shape memory effect of binary NiTi and NiTi based ternary high temperature shape memory alloys. Mater Sci Eng A 2013;560:653–66.
[28] Benafan O, Noebe RD, Padula II SA, Gaydosh DJ, Lerch BA, Garg A, et al. Temperature-dependent behavior of a polycrystalline NiTi shape memory alloy around the transformation regime. Scr Mater 2013;68:571–4.